Crystal structures and superconductivity of carbonaceous sulfur hydrides at pressures up to 300 GPa

Ying Sun,[1] Xue Li,[1] Toshiaki Iitaka,[2] Hanyu Liu,[1,3,4] and Yu Xie[1,3,*]

[1]*International Center for Computational Method & Software and State Key Laboratory of Superhard Materials, College of Physics, Jilin University, Changchun, 130012, China*

[2]*Discrete Event Simulation Research Team, RIKEN Center for Computational Science, 2-1 Hirosawa, Wako, Saitama, 351-0198, Japan*

[3]*Key Laboratory of Physics and Technology for Advanced Batteries (Ministry of Education), College of Physics, Jilin University, Changchun, 130012, China*

[4]*International Center of Future Science, Jilin University, Changchun 130012, China*

(Received 31 December 2021; accepted 18 March 2022; published 4 April 2022)

To explore the crystal structure of the recently claimed room-temperature superconducting carbonaceous sulfur hydrides, we searched for ≈250 000 structures over ≈800 stoichiometries at 300 GPa via advanced crystal structure searching and cluster expansion method. Only several metastable high-temperature superconductors were identified, whose structures can be classified into hydrogen-rich molecular crystals and low-level carbon-doped H_3S-like structures by constructing the ternary phase diagram and simulating the electron-phonon interactions. The C–S–H molecular crystals are composed of CH_4, SH_6, and H_2 molecules, where the superconductivity (with the highest superconducting critical temperature T_c is 156 K found in CSH_{48} at 300 GPa) is mainly contributed to by H_2 units, implying their T_c values are unlikely to be higher than that of metallic molecular hydrogen (T_c of 242 K at 450 GPa). The highest T_c of low-level carbon-doped C–S–H compounds (up to 64 atoms in the primitive cell) at 300 GPa was estimated as 189 K for $H_3S_{0.917}C_{0.083}$. Our results provide a comprehensive map between the crystal structure and superconductivity of carbonaceous sulfur hydride materials at high pressures.

DOI: 10.1103/PhysRevB.105.134501

I. INTRODUCTION

Searching for room-temperature superconductors in hydrides remains a hot topic of intense studies owing to recent theoretical and experimental development under high pressure, particularly the theory-orientated findings of H_3S [1–3] and clathrate superhydrides [4–11], as well as some other predicted potentially high superconducting hydrides [12–15]. In 2020, Snider *et al.* [16] reported the observation of room-temperature superconducting carbonaceous sulfur hydrides, $C_xS_yH_z$, at 288 K and 267 GPa. However, the detailed composition and crystal structure of the superconducting $C_xS_yH_z$ were not reported and remain an open question.

Recent experiments [17,18] on the high-pressure structure and composition of the C–S–H system reported that its structure is complex and different from the common $Im\bar{3}m$–H_3S and other structures predicted and observed for the S–H system. X-ray diffraction (XRD) patterns measured up to 178 GPa identified an orthorhombic structure derived from the Al_2Cu-type determined for $(H_2S)_2H_2$ and $(CH_4)_2H_2$ [18]. However, every material typically experiences several structural transformations when compressed up to a pressure of a few megabars [19], so extrapolating the results from 178 GPa to experimental pressure (up to 267 GPa) is unreliable. Besides, probing light elements that arise in XRD is quite difficult and an accurate structure determination of C–S–H compound at pressures up to 267 GPa is extremely challenging, thus it is necessary to investigate structures of C–S–H compounds theoretically.

Crystal structure prediction method was used to research C–S–H systems at a wide range of pressures (100–250 GPa) [20–22], while no thermodynamically stable ternary compound was found at present. A dynamically stable CSH_7 compound, which can be seen as CH_4 molecules doped in SH_3 host lattice, was proposed to be a high-temperature superconductor with predicted T_c values of up to 194 K at 100 GPa [20,21], which is not in agreement with the measured T_c [16]. Several carbon-doped H_3S compounds with low doping levels were also considered as possible explanations of the room-temperature superconductivity [23–29]. Among of which, a C-doped H_3S compound $H_3S_{0.962}C_{0.038}$ (T_c of 289 K at 260 GPa [23]) was proposed to might be an explanation for the room-temperature superconductivity, whereas the simulation of superconductivity is based on the virtual crystal approximation (VCA) method [30]. It should be noted that the VCA method is employed with linearly mixed pseudopotentials and does not take into account the effect of the doping on the local structure and electronic properties (such as symmetry breaking and local distortions) [26,28]. The T_c calculation of $H_3S_{0.917}C_{0.083}$ using the primitive cell containing 48 atoms shows a relatively low T_c value of ≈170 K at 270 GPa [26], which is quite different from calculation results using VCA [26] and much lower than the experimental values [16]. The

*xieyu@jlu.edu.cn

observed room-temperature superconductivity could not be explained by C–S–H compounds explored so far.

In this work, we performed crystal structure searching of the C–S–H system at 300 GPa via our in-house developed CALYPSO prediction methodology [31–33]. A series of metastable crystals were identified with T_c values $\leqslant$156 K. The coordination number of the C and S atoms in compressed C–S–H crystals are four and six, respectively, with the formation of CH_4 and SH_6 molecules, and the remaining H atoms form H_2 molecules in pairs. The formation of molecular crystals is the fundamental reason for such poor superconductivity. Besides, we searched for ground-state structures of C-doped $Im\bar{3}m$–H_3S using the first-principles cluster expansion method [34]. Superconductivity of $C_xS_{1-x}H_3$ (x = 0.0625, 0.083, and 0.10) was estimated using primitive cells containing 40–64 atoms. The doping was found to lower the density of states at the Fermi level and then decrease the T_c values accordingly. Our results provide a comprehensive map between the crystal structure and superconductivity of carbonaceous sulfur hydride materials at high pressures, which might offer a valuable reference for further exploring the superconducting mechanism.

II. COMPUTATIONAL DETAILS

Universal variable-composition structure searches for $C_xS_yH_z$ (x = 1–5, y = 1–5, z = 1–48) was performed at 300 GPa with the CALYPSO structure prediction method [31–33], using simulation cells that consist of a maximal number of 60 atoms. In total, 798 different compositions, where more than 300 structures for each stoichiometry, have been studied. The energetic stability of different $C_xS_yH_z$ stoichiometries are evaluated by their formation enthalpy of dissociated into the most competing element and binary compounds. Here the enthalpies for competing compounds are calculated separately from their stable phases [2,35–38] at 300 GPa. For compositions with formation enthalpies lower than 50 meV/atom, further fixed-composition structural predictions were conducted to ensure the calculation reached convergence. For most cases, the structure search for each chemical composition converges (evinced by a lack of any additional structure with lower energy) after 1000–1200 structures were investigated. The C-doped $Im\bar{3}m$–H_3S compounds was explored by cluster expansion [34], as implemented in the alloy-theoretic automated toolkit (ATAT) [39].

The underlying structural relaxation and computations of enthalpy, phonon, and electronic structures were all performed in the framework of density-functional theory (DFT) as implemented in the Vienna *Ab Initio* Simulation Package (VASP) [40], with an energy convergence threshold of 1×10^{-5} eV per cell. The electron-ion interaction was described by projector-augmented-wave (PAW) [41] potentials with the $2s^22p^2$, $3s^23p^4$, and $1s^1$ configurations treated as valence electrons for C, S, and H, respectively. The generalized gradient approximation (GGA) [42] in the scheme of Perdew-Burke-Ernzerhof (PBE) [43] was chosen for the exchange-correlation functional, and kinetic cutoff energy of 900 eV and Monkhorst-Pack $\boldsymbol{k}$ meshes with a grid spacing of 0.20 $Å^{-1}$ were then adopted to ensure a satisfactory degree of convergence was achieved. Iterative relaxation of atomic positions was stopped when the forces generally acting on the atoms were found to be smaller than 0.01 eV/Å. With this criterion, the change in total energy between successive steps was less than 0.01 meV/cell. The electron localization function (ELF) [44] was used to describe and visualize chemical bonds in molecules and solids, and the isosurface plots at ELF = 0.75 (a typical good number for characterization of covalent bondings) was used to clearly illustrate the covalent bonding nature and confirm the formation of CH_4, SH_6, and H_2 molecules in C–S–H compounds.

The electron-phonon coupling (EPC) calculations were carried out using the QUANTUM ESPRESSO code [45]. Ultrasoft pseudopotentials [46] for C, S, and H were used with a kinetic-energy cutoff for wave functions of 80 Ry and a kinetic-energy cutoff for charge density and potential of 1000 Ry. Here, q-point meshes with 10–20 irreducible q points were used for each C–S–H ternaries to compute the EPC matrix elements. For H_3S, the EPC matrix elements were computed in the first BZ on $8 \times 8 \times 8$ q meshes using individual EPC matrices obtained with a $16 \times 16 \times 16$ k points mesh. Electron-phonon couplings (EPC) constant λ, $\omega_{\log}$, and T_c are solved using the elk code [47]. T_c are estimated using the isotropic Migdal-Eliashberg theory [48], which gives us the superconducting gap as a function of temperature. The highest temperature for which superconducting gap value is nonzero defines the T_c.

III. RESULTS AND DISCUSSION

Based on the results from the variable-composition crystal structure searches and the cluster expansion, we constructed the ternary phase diagram of C–S–H as presented in Fig. 1(a). Unfortunately, no thermodynamically stable C–S–H compounds were found, indicating all the ternary compounds tend to decompose into elements and binaries under certain conditions. Nevertheless, in previous high-throughput material discovery studies, the convention for the threshold between metastable (likely to be synthesized) and unstable (unlikely to be synthesized) compounds is 50 meV/atom [49]. The same convention was adopted in this work. Therefore, metastable C–S–H compounds cannot be precluded from experimental synthesis.

We found that C–S–H compounds with high-H content or a low level of carbon doping are more stable than other compositions. Specifically, there are ten H-rich ternaries and four low-level C-doping compounds that are metastable with formation enthalpies lower than 50 meV/atom at 300 GPa [as shown in Fig. 1(b), formation enthalpies and structural parameters of these metastable compounds are listed in Table S1 [50]]. Among of which $P3$–C_2SH_{14} has the lowest enthalpy of decomposition at 300 GPa [10 meV/atom above the convex hull, as shown in Fig. 1(b)]. Further pressure may help to reduce the formation enthalpy and stabilize the new compound [19], calculated formation enthalpy as a function of pressure is thus shown in Fig. S1, which shows that $P3$–C_2SH_{14} is not a thermodynamically stable structure at a wide range of pressures (200–400 GPa), and has the lowest enthalpy value of thermal decomposition of 6 meV/atom at 270 GPa. Then we focus on the crystal structures and superconductivity of the H-rich compounds.

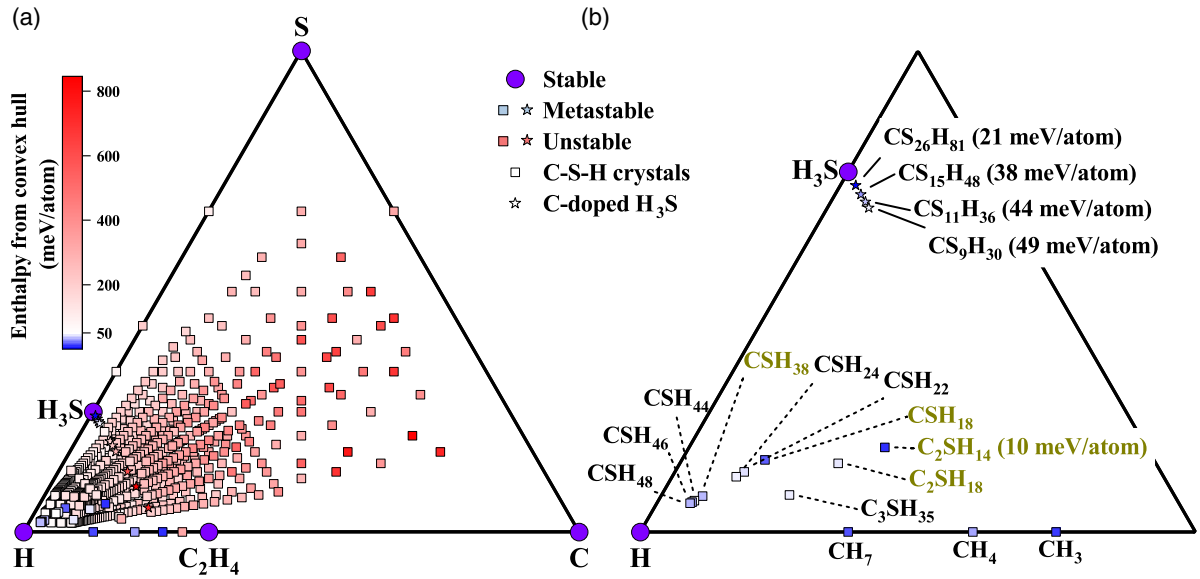

FIG. 1. (a) Calculated stabilities of $C_xS_yH_z$ relative to C, S, H, and binary compounds at 300 GPa. H-rich molecular crystals and H_3S-like structures with low levels of carbon doping are presented with squares and stars, respectively. A square (or star) filling with blue or red indicates that the corresponding ternary compound is metastable or unstable. Purple circles indicate stable phases. (b) Metastable C–S–H compounds with formation enthalpies below 50 meV/atom at 300 GPa. Labels in gold or black indicate the corresponding ternary compounds are insulated or metallic.

These metastable H-rich C–S–H compounds are all molecule crystals composed of CH_4, SH_6, and H_2 units. C atoms form CH_4 molecule with neighboring H atoms. The valence electron configuration of the S atom is $3s^2 3p^4$, which makes it not surprising that the coordination number of S is six at 300 GPa, and then results in SH_6 molecule units. Other H atoms form H_2 molecules in pairs. Such molecule crystals are usually insulators and hard to be good conductors though insulation-metal phase transition may occur under high pressure. Calculations show that C_2SH_{14}, CSH_{18}, CSH_{38}, and C_2SH_{18} exhibit nonmetallic characteristics at 300 GPa with band gaps of 1.65, 0.21, 0.27, and 0.79 eV, respectively, while the other six metastable molecular crystals are metallic with $T_c \leqslant 156$ K (as shown in Table I). We discuss the structures and superconductivity of the most stable C_2SH_{14} and the highest superconducting CSH_{48} as representatives of H-rich molecular crystals.

TABLE I. Space group (S.G.), formation enthalpy (ΔE, meV/atom), band gap (gap, eV), electronic density of states at the Fermi level [$N(E_f)$, states/spin/Ry/f.u.], λ, $\omega_{\log}$ (K), and T_c (K) estimated using $\mu^\star = 0.10(0.13)$ for metastable C–S–H molecular crystals at 300 GPa [(M) indicates metallic phase].

Compound	S.G.	ΔE	Gap	$N(E_f)$	λ	$\omega_{\log}$	T_c
C_2SH_{14}	$P3$	10	1.65				
CSH_{18}	Cm	18	0.21				
CSH_{46} (M)	$P1$	32		4.62	0.97	1293	93(80)
CSH_{48} (M)	$P1$	35		7.58	1.56	1071	156(142)
CSH_{38}	$P1$	36	0.27				
CSH_{22} (M)	$P1$	44		2.64	0.99	1045	78(68)
C_2SH_{18}	$P\bar{1}$	45	0.79				
C_3SH_{35} (M)	$P1$	46		6.59	2.47	558	156(143)
CSH_{24} (M)	$P1$	47		4.34	2.09	595	138(125)
CSH_{44} (M)	$P1$	50		5.51	1.50	791	113(100)

Crystal structures of $P3$–C_2SH_{14} and $P1$–CSH_{48} are shown in Figs. 2(a) and 2(b), where the characteristics of molecular crystals are so obvious that they can be written as $(CH_4)_2(SH_6)$ and $(CH_4)(SH_6)(H_2)_{19}$, respectively. To clarify the origin of metallic properties in $P1$–CSH_{48}, electron band structures and the project electronic density of states (PDOS) of insulating $P3$–C_2SH_{14} and metallic $P1$–CSH_{48} at 300 GPa is shown in Figs. 2(c) and 2(d). Calculated results show that CH_4 and SH_6 contribute more to the deep orbitals with lower energy due to there are strong covalent bonding behavior in C–H and S–H bonds, while hydrogen atoms make a substantial contribution to the electronic density of states near the Fermi level [$N(E_f)$], indicating that the existence of a large number of H_2 units in the $P1$–CSH_{48} compound results in its metallic property. EPC calculations show an integrated electron-phonon coupling parameter λ of 1.56 at 300 GPa, which is not very large compared with the value of $\lambda = 2.2$ for H_3S [2]. 90% of the contribution to λ is derived from the H − H vibration modes of 250–2200 cm^{-1} [as shown in Fig. 2(e)]. T_c values of the H_2-rich hydrides, such as MgH_{16} and YH_{24}, usually not higher than that of the molecular hydrogen (T_c of ≈242 K at 450 GPa [51,52]). Similarly, with a direct numerical solution to the Eliashberg equations, T_c of $P1$–CSH_{48} is estimated to be 142–156 K at 300 GPa, where the Coulomb pseudopotential was set to be the typical values of $\mu^\star = 0.10$–0.13. Table shows a positive correlation between λ, $N(E_f)$, and the hydrogen content of C–S–H molecular crystals, which is consistent with the fact that the metallic and superconductivity of C–S–H molecular crystals are mainly due to the contribution of H_2 molecules. Naturally, $P1$–CSH_{48}, with the highest hydrogen content, has

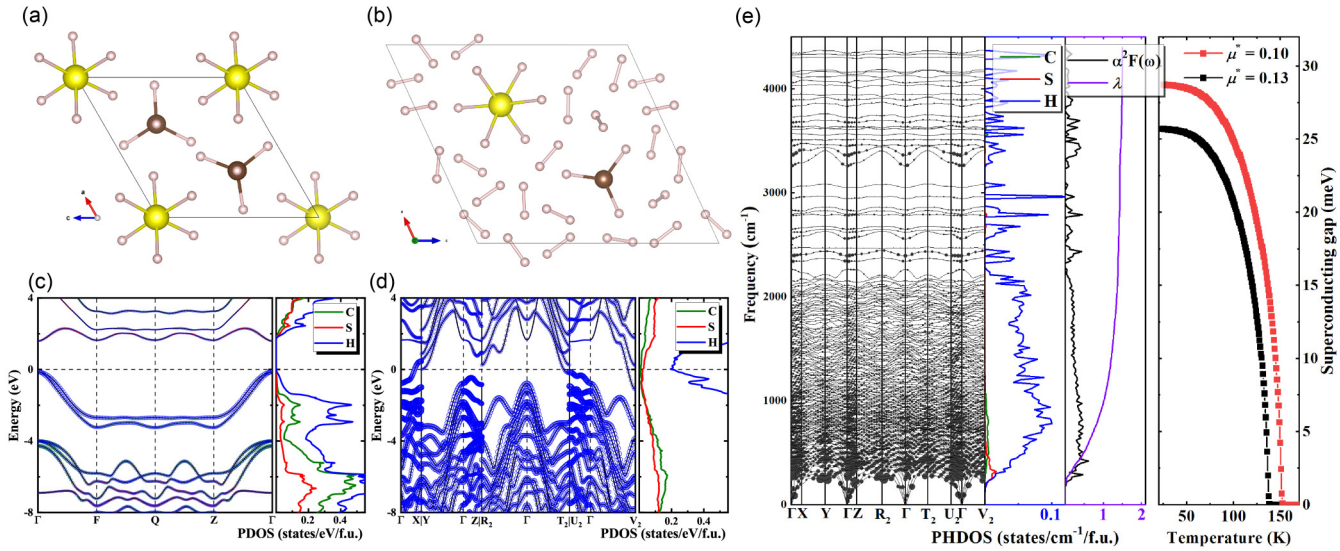

FIG. 2. Crystal structures of (a) $P3$–C_2SH_{14} and (b) $P1$–CSH_{48} at 300 GPa. The large, medium, and small spheres represent the S, C, and H atoms, respectively. CH_4, SH_6, and H_2 molecules are building units that form these two molecule crystals. Electronic band structure (left panel) and projected density of states (right panel) of (c) $P3$–C_2SH_{14} and (d) $P1$–CSH_{48} at 300 GPa. (e) Phonon dispersion curves with the strength of q-resolved λ_q indicated by circle size, projected phonon densities of states (PHDOS), isotropic Eliashberg spectral function $\alpha^2F(\omega)$ and EPC parameter $\lambda(\omega)$, and superconducting gap of $P1$–CSH_{48} at 300 GPa.

the highest $N(E_f)$ and thus the highest T_c value (156 K) among the six metallic molecular crystals listed in Table I.

Next, we investigated the four metastable H_3S-like compounds with 3.7%, 6.25%, 8.3%, and 10% doped carbon, respectively, which were identified using the cluster expansion method. Primitive cells of these four H_3S-like compounds can be seen as supercells of the $Im\bar{3}m$–H_3S where sulfur atoms were replaced by carbon atoms. Thus, carbon atoms here are octahedrally coordinated by six hydrogen atoms (as shown in Fig. 3). Low-level carbon-doping localizes electrons in C–H bonds and reduced symmetry, which is detrimental to high-temperature superconductivity. To investigate how different levels of carbon doping affect the stability, electronic structure, and superconductivity of C–S–H compounds, detailed analysis were carried out on the $Pm\bar{3}m$–$H_3S_{0.9375}C_{0.0625}$ ($CS_{15}H_{48}$), $C2/m$–$H_3S_{0.917}C_{0.083}$ ($CS_{11}H_{36}$), and $C2/m$–$H_3S_{0.9}C_{0.1}$ (CS_9H_{30}) stoichiometries, since the electron-phonon coupling simulations of $Im\bar{3}m$–$H_3S_{0.963}C_{0.037}$ ($CS_{26}H_{81}$) exceed the limits of our current computing facilities. All of these three compounds are dynamically stable at 300 GPa and can be dynamically stable at pressures down to 260, 230, and 180 GPa, respectively (see Fig. S2 for detail).

Calculated superconductivity of compressed $CS_{15}H_{48}$, $CS_{11}H_{36}$, and CS_9H_{30} is listed in Table II. To better visualize how doping affect superconductivity, $N(E_f)$, λ, and T_c (K) for C-doped H_3S compounds with different doping ratios at 300 GPa are shown in Fig. 4(a). With the increase of C-doping concentration, T_c rises first and then decreases. $CS_{11}H_{36}$ with a C-doped concentration of 8.3% has the highest T_c value. It is worth noting that, with the increase of doping concentration, T_c shows exactly the same trend as $N(E_f)$, which indicated that doping affects the $N(E_f)$ thus T_c values. Additionally, the superconducting temperature increases with decreasing pressure [as shown in Fig. 4(b)], and $CS_{11}H_{36}$ have the T_c value of 216 K at 230 GPa. Notably, the T_c values of C-doped H_3S compounds are lower than that of H_3S in the pressure range studied and are ≈100 K lower than the maximum measured value for the C–S–H superconductor [16], which is inconsistent with previous studies [25,26,28].

Despite performing thorough chemical composition and crystal structure searches for the C–S–H system at 300 GPa

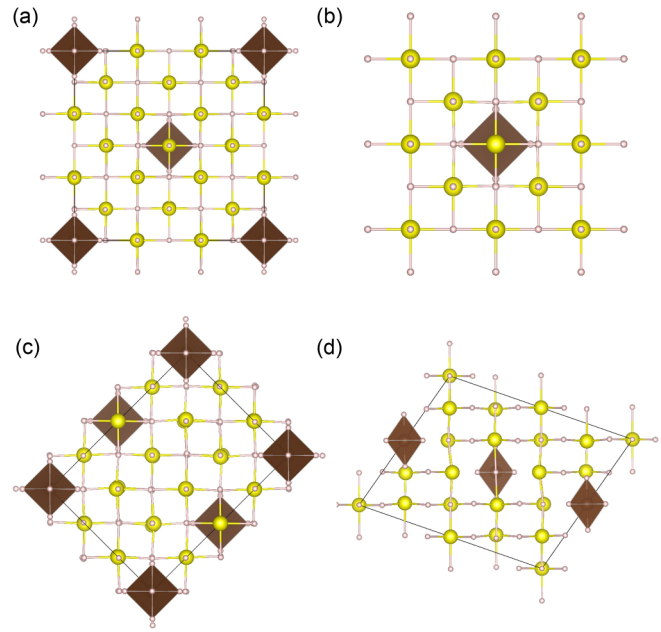

FIG. 3. Crystal structures of (a) $Im\bar{3}m$–$H_3S_{0.963}C_{0.037}$ ($CS_{26}H_{81}$), (b) $Pm\bar{3}m$–$H_3S_{0.9375}C_{0.0625}$ ($CS_{15}H_{48}$), (c) $C2/m$–$H_3S_{0.917}C_{0.083}$ ($CS_{11}H_{36}$), and (d) $C2/m$–$H_3S_{0.9}C_{0.1}$ (CS_9H_{30}) at 300 GPa. The large, medium, and small spheres represent the S, C, and H atoms, respectively. The translucent regular tetrahedrons represent the SH_6-like CH_6 units.

TABLE II. Primitive cells, space group (S.G.), pressure (GPa), electronic density of states at the Fermi level [$N(E_f)$, states/spin/Ry/f.u.], λ, $\omega_{\log}$ (K), isotropic superconducting gap (meV) at 40 K, and T_c (K) estimated using $\mu^\star = 0.10(0.13)$ for H_3S and H_3S-like low-level C-doping C–S–H compounds.

Compound	Primitive cell	S.G.	Pressure	$N(E_f)$	λ	$\omega_{\log}$	Δ	T_c
H_3S	H_3S	$Im\bar{3}m$	180	3.30	2.35	1134	51.32	245(230)
H_3S	H_3S	$Im\bar{3}m$	200	3.31	1.83	1366	45.68	233(217)
H_3S	H_3S	$Im\bar{3}m$	300	3.48	1.30	1679	35.26	199(178)
$H_3S_{0.9375}C_{0.0625}$	$CS_{15}H_{48}$	$Pm\bar{3}m$	260	3.18	1.74	900	35.07	190(168)
$H_3S_{0.9375}C_{0.0625}$	$CS_{15}H_{48}$	$Pm\bar{3}m$	300	3.14	1.30	1353	30.29	168(151)
$H_3S_{0.917}C_{0.083}$	$CS_{11}H_{36}$	$C2/m$	230	3.26	1.80	1176	41.23	216(200)
$H_3S_{0.917}C_{0.083}$	$CS_{11}H_{36}$	$C2/m$	300	3.18	1.47	1338	35.30	189(172)
$H_3S_{0.9}C_{0.1}$	CS_9H_{30}	$C2/m$	180	3.12	1.84	1104	38.79	201(187)
$H_3S_{0.9}C_{0.1}$	CS_9H_{30}	$C2/m$	300	3.01	1.29	1429	31.17	169(153)

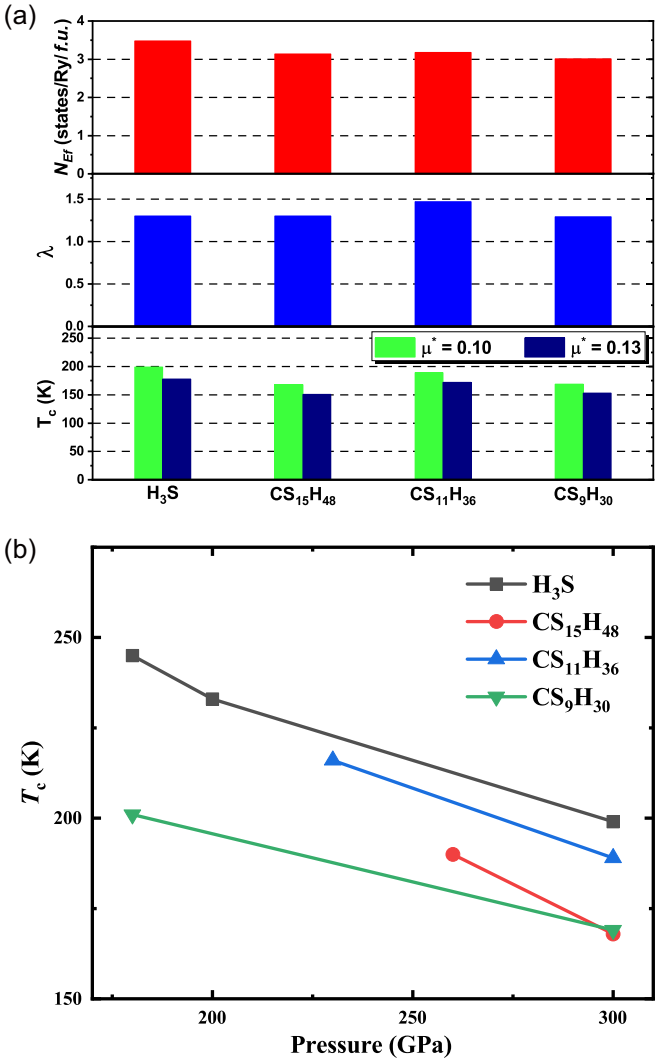

FIG. 4. (a) Calculated electronic density of states at the Fermi level [$N(E_f)$] (top panel), the electron-phonon coupling parameter (λ) (middle panel), and T_c (bottom panel) of H_3S and H_3S-like low level C-doping C–S–H compounds at 300 GPa. (b) Pressure dependence of T_c of H_3S and H_3S-like low level C-doping C–S–H compounds.

to tackle the unsolved puzzle of room-temperature superconducting carbonaceous sulfur hydride, neither a thermodynamically stable compound nor room-temperature superconductivity was identified. We have to mention that the validity of the experimental results has recently been questioned [53–55], where it has been proposed that either the measured superconductivity in C–S–H might be unconventional or the measurements might be erroneous. Clearly, more effort is required to fully understand the measured superconductivity in carbonaceous sulfur hydride.

IV. CONCLUSION

In summary, we have extensively explored the phase space of carbonaceous sulfur hydrides at 300 GPa by using the CALYPSO structure prediction and cluster expansion method. Although no thermodynamically stable phase was found, several metastable crystals have been identified to be high-temperature superconductors with T_c values of 100–200 K. The coordination number of the C and S atoms in H-rich metastable C– S– H crystals are four and six, respectively, with the formation of CH_4 and SH_6 units, where the remaining H atoms form H_2 units in pairs. Such kinds of molecular crystals are apparently not good candidates for room-temperature superconductors. Using primitive cells up to 64 atoms, T_c values of H_3S-like structures with low levels of carbon doping were estimated to be $\leqslant$189 K for $H_3S_{0.917}C_{0.083}$ at 300 GPa, for the reason that doping localizes electrons in C–H bonds and then decreases the $N(E_f)$. Our current results provide a comprehensive map between the crystal structure and superconductivity of carbonaceous sulfur hydride materials at high pressures. More efforts, both theoretically and experimentally, are required to be done for making the mechanism of room-temperature superconducting in carbonaceous sulfur hydride clear.

ACKNOWLEDGMENTS

This work was supported by the National Key Research and Development Program of China (Grant No. 2021YFA1400203), the Major Program of the National Natural Science Foundation of China (Grant No. 52090024), the National Natural Science Foundation of China (Grants No.

12074138, No. 11534003, and No. 11974134), the China Postdoctoral Science Foundation (Grants No. 2020M681032 and No. 2021T140264), the Key Program of the National Natural Science Foundation of China (Grant No. 22131006), and the Strategic Priority Research Program of Chinese Academy of Sciences (Grant No. XDB33000000). The calculation was performed in the computing facilities at the HOKUSAI system at RIKEN (Japan).

[1] Y. Li, J. Hao, H. Liu, Y. Li, and Y. Ma, J. Chem. Phys. **140**, 174712 (2014).
[2] D. Duan, Y. Liu, F. Tian, D. Li, X. Huang, Z. Zhao, H. Yu, B. Liu, W. Tian, and T. Cui, Sci. Rep. **4**, 6968 (2014).
[3] A. P. Drozdov, M. I. Eremets, I. A. Troyan, V. Ksenofontov, and S. I. Shylin, Nature (London) **525**, 73 (2015).
[4] H. Liu, I. I. Naumov, R. Hoffmann, N. W. Ashcroft, and R. J. Hemley, Proc. Natl. Acad. Sci. USA **114**, 6990 (2017).
[5] F. Peng, Y. Sun, C. J. Pickard, R. J. Needs, Q. Wu, and Y. Ma, Phys. Rev. Lett. **119**, 107001 (2017).
[6] H. Liu, I. I. Naumov, Z. M. Geballe, M. Somayazulu, J. S. Tse, and R. J. Hemley, Phys. Rev. B **98**, 100102(R) (2018).
[7] A. P. Drozdov, P. P. Kong, V. S. Minkov, S. P. Besedin, M. A. Kuzovnikov, S. Mozaffari, L. Balicas, F. F. Balakirev, D. E. Graf, V. B. Prakapenka *et al.*, Nature (London) **569**, 528 (2019).
[8] M. Somayazulu, M. Ahart, A. K. Mishra, Z. M. Geballe, M. Baldini, Y. Meng, V. V. Struzhkin, and R. J. Hemley, Phys. Rev. Lett. **122**, 027001 (2019).
[9] J. Lv, Y. Sun, H. Liu, and Y. Ma, Matter Radiat. Extrem. **5**, 068101 (2020).
[10] L. Boeri, R. Hennig, P. Hirschfeld, G. Profeta, A. Sanna, E. Zurek, W. E. Pickett, M. Amsler, R. Dias, M. I. Eremets, C. Heil, R. J. Hemley, H. Liu, Y. Ma, C. Pierleoni, A. N. Kolmogorov, N. Rybin, D. Novoselov, V. Anisimov, A. R. Oganov *et al.*, J. Phys.: Condens. Matter **34**, 183002 (2022).
[11] Y. Sun, H. Liu, and Y. Ma, Acta Phys. Sin. **70**, 017407 (2021).
[12] Y. Sun, J. Lv, Y. Xie, H. Liu, and Y. Ma, Phys. Rev. Lett. **123**, 097001 (2019).
[13] J. A. Flores-Livas, L. Boeri, A. Sanna, G. Profeta, R. Arita, and M. Eremets, Phys. Rep. **856**, 1 (2020).
[14] K. P. Hilleke and E. Zurek, J. Appl. Phys. **131**, 070901 (2022).
[15] X. Zhong, J. S. Tse, R. J. Hemley, and H. Liu, The Innovation **3**, 100226 (2022).
[16] E. Snider, N. Dasenbrock-Gammon, R. McBride, M. Debessai, H. Vindana, K. Vencatasamy, K. V. Lawler, A. Salamat, and R. P. Dias, Nature (London) **586**, 373 (2020).
[17] E. Bykova, M. Bykov, S. Chariton, V. B. Prakapenka, K. Glazyrin, A. Aslandukov, A. Aslandukova, G. Criniti, A. Kurnosov, and A. F. Goncharov, Phys. Rev. B **103**, L140105 (2021).
[18] A. Lamichhane, R. Kumar, M. Ahart, N. P. Salke, N. Dasenbrock-Gammon, E. Snider, Y. Meng, B. Lavina, S. Chariton, V. B. Prakapenka, M. Somayazulu, R. P. Dias, and R. J. Hemley, J. Chem. Phys. **155**, 114703 (2021).
[19] L. Zhang, Y. Wang, J. Lv, and Y. Ma, Nat. Rev. Mater. **2**, 17005 (2017).
[20] Y. Sun, Y. Tian, B. Jiang, X. Li, H. Li, T. Iitaka, X. Zhong, and Y. Xie, Phys. Rev. B **101**, 174102 (2020).
[21] W. Cui, T. Bi, J. Shi, Y. Li, H. Liu, E. Zurek, and R. J. Hemley, Phys. Rev. B **101**, 134504 (2020).
[22] M. Gubler, J. A. Flores-Livas, A. Kozhevnikov, and S. Goedecker, Phys. Rev. Materials **6**, 014801 (2022).
[23] Y. Ge, F. Zhang, R. P. Dias, R. J. Hemley, and Y. Yao, Mater. Today Phys. **15**, 100330 (2020).
[24] S. Hu, R. Paul, V. Karasiev, and R. Dias, arXiv:2012.10259.
[25] X. Wang, T. Bi, K. P. Hilleke, A. Lamichhane, R. J. Hemley, and E. Zurek, arXiv:2109.09898.
[26] T. Wang, M. Hirayama, T. Nomoto, T. Koretsune, R. Arita, and J. A. Flores-Livas, Phys. Rev. B **104**, 064510 (2021).
[27] X. H. Zheng and J. X. Zheng, Solid State Commun. **331**, 114295 (2021).
[28] H. Guan, Y. Sun, and H. Liu, Phys. Rev. Research **3**, 043102 (2021).
[29] Z. Shao, H. Song, H. Yu, and D. Duan, J. Supercond. Nov. Magn. (2021), doi: 10.1007/s10948-021-06061-z.
[30] L. Nordheim, Ann. Phys. (Berlin, Ger.) **401**, 607 (1931).
[31] Y. Wang, J. Lv, L. Zhu, and Y. Ma, Phys. Rev. B **82**, 094116 (2010).
[32] Y. Wang, J. Lv, L. Zhu, and Y. Ma, Comput. Phys. Commun. **183**, 2063 (2012).
[33] B. Gao, P. Gao, S. Lu, J. Lv, Y. Wang, and Y. Ma, Sci. Bull. **64**, 301 (2019).
[34] J. M. Sanchez, F. Ducastelle, and D. Gratias, Phys. A (Amsterdam, Neth.) **128**, 334 (1984).
[35] C. J. Pickard and R. J. Needs, Nat. Phys. **3**, 473 (2007).
[36] H. Liu, I. I. Naumov, and R. J. Hemley, J. Phys. Chem. Lett. **7**, 4218 (2016).
[37] Y. Li, L. Wang, H. Liu, Y. Zhang, J. Hao, C. J. Pickard, J. R. Nelson, R. J. Needs, W. Li, Y. Huang, I. Errea, M. Calandra, F. Mauri, and Y. Ma, Phys. Rev. B **93**, 020103(R) (2016).
[38] N. Zarifi, H. Liu, and J. S. Tse, Sci. Rep. **5**, 10458 (2015).
[39] A. van de Walle, M. Asta, and G. Ceder, CALPHAD: Comput. Coupling Phase Diagrams Thermochem. **26**, 539 (2002).
[40] G. Kresse and J. Furthmüller, Phys. Rev. B **54**, 11169 (1996).
[41] P. E. Blöchl, Phys. Rev. B **50**, 17953 (1994).
[42] J. P. Perdew and Y. Wang, Phys. Rev. B **45**, 13244 (1992).
[43] J. P. Perdew, K. Burke, and M. Ernzerhof, Phys. Rev. Lett. **77**, 3865 (1996).
[44] A. D. Becke and K. E. Edgecombe, J. Chem. Phys. **92**, 5397 (1990).
[45] P. Giannozzi, S. Baroni, N. Bonini, M. Calandra, R. Car, C. Cavazzoni, D. Ceresoli, G. L. Chiarotti, M. Cococcioni, I. Dabo *et al.*, J. Phys.: Condens. Matter **21**, 395502 (2009).
[46] D. Vanderbilt, Phys. Rev. B **41**, 7892 (1990).
[47] The ELK code, url: http://elk.sourceforge.net/.
[48] J. R. Schrieffer, *Theory of Superconductivity* (CRC Press, Boca Raton, 2018).
[49] H. Xiao, Y. Dan, B. Suo, and X. Chen, J. Phys. Chem. C **124**, 2247 (2020).
[50] See Supplemental Material at http://link.aps.org/supplemental/10.1103/PhysRevB.105.134501 for phonon dispersion curves and structural parameters of all predicted metastable ternary compounds.

[51] L. Zhang, Y. Niu, Q. Li, T. Cui, Y. Wang, Y. Ma, Z. He, and G. Zou, Solid State Commun. **141**, 610 (2007).
[52] P. Cudazzo, G. Profeta, A. Sanna, A. Floris, A. Continenza, S. Massidda, and E. K. U. Gross, Phys. Rev. Lett. **100**, 257001 (2008).
[53] J. E. Hirsch and F. Marsiglio, Phys. Rev. B **103**, 134505 (2021).
[54] E. Talantsev, Supercond. Sci. Technol. **34**, 034001 (2021).
[55] M. Dogan and M. L. Cohen, Phys. C (Amsterdam, Neth.) **583**, 1353851 (2021).